Sentinel data for critical raw materials (CRM) exploration: first results of the S34I project

Joana Cardoso-Fernandes, Morgana Carvalho, Antonio Azzalini, Gonçalo Rodrigues, Gonçalo Monteiro, et al.

Joana Cardoso-Fernandes, Morgana Carvalho, Antonio Azzalini, Gonçalo Rodrigues, Gonçalo Monteiro, Alexandre Lima, Ana Cláudia Teodoro, "Sentinel data for critical raw materials (CRM) exploration: first results of the S34I project," Proc. SPIE 12734, Earth Resources and Environmental Remote Sensing/GIS Applications XIV, 127340W (19 October 2023); doi: 10.1117/12.2679373

SPIE.

Event: SPIE Remote Sensing, 2023, Amsterdam, Netherlands

Sentinel data for critical raw materials (CRM) exploration: first results of the S34I project

Joana Cardoso-Fernandes[a,b]*, Morgana Carvalho[a], Antonio Azzalini[a], Gonçalo Rodrigues[a], Gonçalo Monteiro[a], Alexandre Lima[a,b], Ana Cláudia Teodoro[a,b]
[a] Department of Geosciences, Environment and Spatial Planning, Faculty of Sciences, University of Porto, Rua Campo Alegre, 4169-007 Porto, Portugal; [b] ICT (Institute of Earth Sciences)–Porto pole (Portugal), Rua Campo Alegre, 4169-007 Porto, Portugal

ABSTRACT

To achieve sustainable development goals, it is crucial to ensure the best practices through the whole mining cycle of critical raw materials (CRM) used in high-tech, low-carbon goods (batteries, wind turbines, electronics). This is the aim of the SECURE AND SUSTAINABLE SUPPLY OF RAW MATERIALS FOR EU INDUSTRY (S34I) Horizon Europe (HE) project that began on January 1st, 2023. S34I is investigating new data-driven methods to analyze Earth Observation (EO) data, supporting systematic mineral exploration (and other) activities to increase European autonomy regarding CRM resources. The S34I project is based on satellite data, airborne, unmanned aerial vehicle (UAV), ground-based conventional in-situ techniques/methods, and fieldwork. This study presents the first preliminary results based on Sentinel-1 and Sentinel-2 data using classical image processing techniques (RGB combinations, band ratio, Principal Component Analysis – PCA, and unsupervised classification) for mineral exploration in Spain, either: (i) on land (Aramo area), to gain knowledge on cobalt (Co) deposits (and associate CRMs) by hydrothermal alteration mapping; and (ii) offshore/shallow waters (Ria de Vigo area), to update the knowledge on coastal metallic placers including CRMs such as Ti, Sn, Li, rare earth elements (REEs) and Au. Among the techniques, PCA proved most effective, followed by band ratios, and self-proposed algorithms for detecting placer minerals showed promise, warranting further investigation. In the future, S34I will exploit Copernicus Contributing Missions (CCM) and other EU hyperspectral satellite sensors such as PRISMA and EnMAP. Different Artificial Intelligence (AI) techniques will, in the future, promote advances and innovative methods that mining stakeholders can use to address the challenges faced in different phases of the mining life-cycle.

Keywords: Earth Observation, Copernicus, raw materials, land, coastal areas, cobalt, hydrothermal alteration, satellite

1. INTRODUCTION

The battery market, primarily driven by the automotive sector, is experiencing exponential growth. The long-term trend of increased electric vehicle sales presents opportunities for the entire battery supply chain, including Cobalt (Co). Benchmark Mineral Intelligence predicted for 2023 a lithium demand reaching 900,000 tonnes that can increase to 1.5 million tonnes in 2026, along with significant Co shortages expected from 2030[1]. This surge in demand is also reflected in Co prices, which have reached their highest levels in three years. Within the scope of the SECURE AND SUSTAINABLE SUPPLY OF RAW MATERIALS FOR EU INDUSTRY (S34I) Horizon Europe (HE) project (https://s34i.eu/), Aramo and Rias Baixas serve as pilot sites that offer different instances of Critical Raw Materials (CRM) as subjects of study.

Optical, thermal, and Synthetic Aperture Radar (SAR) remote sensing data have been used in geological exploration and extraction activities allowing to target exploration areas and monitoring extraction works[2]. Regarding optical and thermal remote sensing, Landsat and ASTER data lead the applications in mining and related geological task, mainly due to a better spectral resolution in the short-wave infrared (SWIR) and thermal infrared (TIR), increasing the lithological and mineral mapping potentialities[3]. More recently, Earth Observation (EO) data from Copernicus satellite sensors, such as Sentinel-2, played an increasingly significant role in mineral mapping[4]. SAR data (such as Sentinel-1) are typically used to map structural elements[5], but SAR can also be used for lithological mapping due to variations in outcrop patterns and the size and frequency of coarse rock detritus[6].

*joana.fernandes@fc.up.pt

Earth Resources and Environmental Remote Sensing/GIS Applications XIV, edited by Karsten Schulz, Ulrich Michel, Konstantinos G. Nikolakopoulos, Proc. of SPIE Vol. 12734, 127340W
 · 0277-786X · doi: 10.1117/12.2679373

Thus, this works presents a preliminary attempt to use Copernicus Sentinel data to identify potential areas for CRM deposits, namely Co in the Aramo area (Spain) and metallic placers in Rias Baixas (Spain). The main objective can be divided into specific objectives, namely: (i) assess the suitability of Sentinel-1 and Sentinel-2 data, and (ii) compare the performance of classical image processing techniques for Co-related hydrothermal alteration and metallic placers mapping. For that purpose, literature-based and self-proposed inputs for RGB combinations, band ratios, Principal Component Analysis (PCA), and unsupervised classification (K-means clustering algorithm) were tested in both study cases.

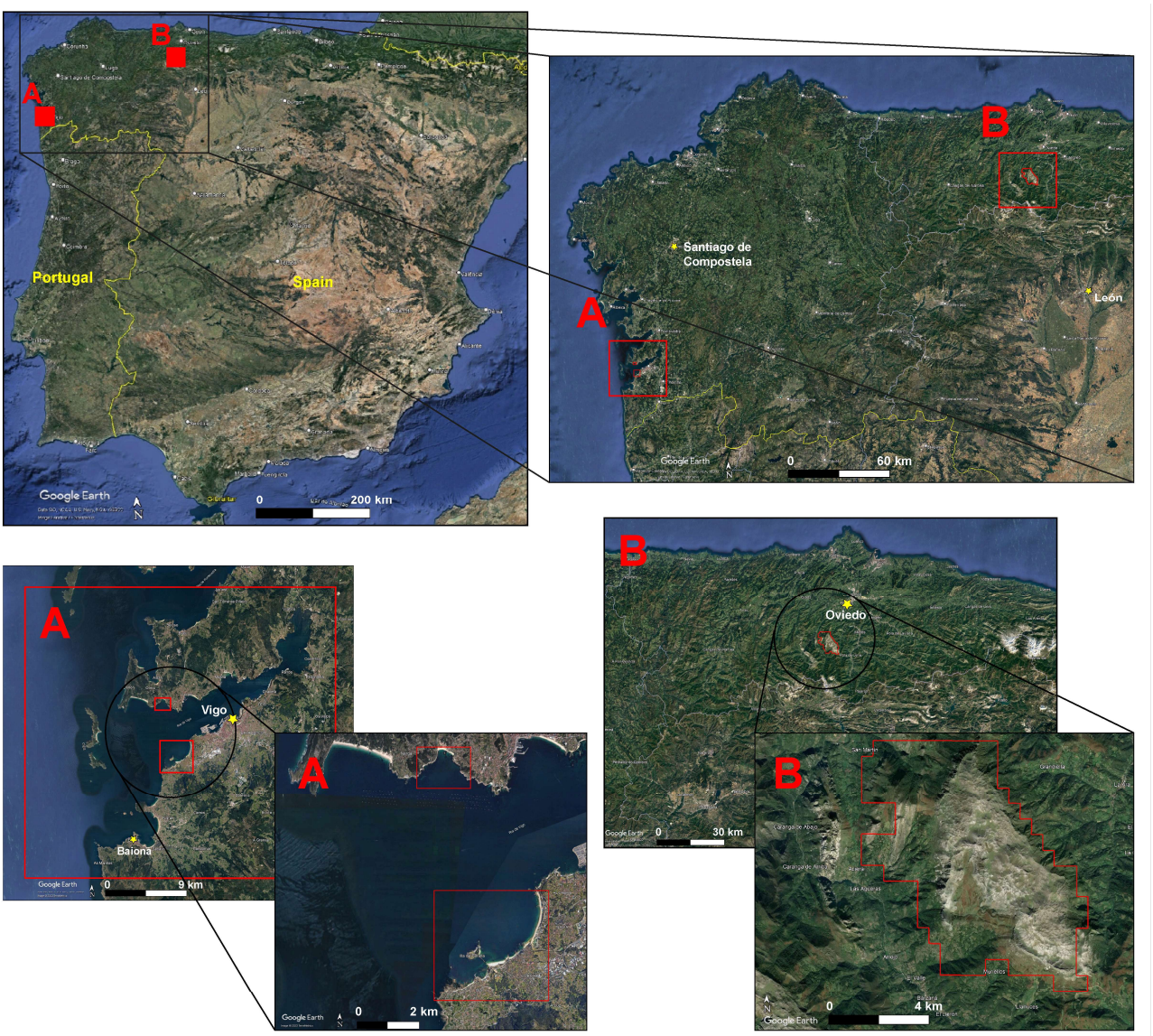

Figure 1. Location of the two case study areas in the Iberian Peninsula, northwest of Spain. A: Rias Baixas area (encompassing Vigo). B: Aramo area (encompassing Oviedo).

1.1 Aramo area

The Aramo mine is situated in the northern region of Spain and the northern part of the Iberian Peninsula, specifically within the Province of Asturias. The selected area consists of a raised, relatively flat plateau with sparse vegetation. The mineralization style observed is epithermal (epigenetic), specifically Cobalt-Copper-Nickel mineralization. This mineralization is found within specific stratigraphic limestone units of the Upper Namurian period in the Carboniferous Period[7]. The mineralization is controlled by significant Late Variscan structural controls, associated with both East-West and North-South faults and fractures. The mineralization exhibits intense hydrothermal alteration in the form of

dolomitization, occurring in multiple phases[8, 9]. Additionally, there are silicification and argillic processes linked to the primary mineralized bodies, which introduce a broader level of alteration. This alteration results in spectral and compositional variation and contrast, providing a basis for the proposed remote sensing study. The mineralization consists of oxides, sulphides, and sulphoarsenides of Cobalt-Copper-Nickel[10].

1.2 Rias Baixas area

Rias Baixas is situated on the southwestern coast of Galicia, in northwestern Spain. It is a funnel-shaped estuary called *Ria*. There are several occurrences of *Rias* on Galicia's coastline, that lies within the Hercynian orogenic belt and developed during the Holocene period[11]. There are limited and relatively thin sedimentary formations from the Quaternary period. These formations primarily consist of terrace sediments, tidal flats, marshes, beaches, and dunes[12]. They develop on a substrate of igneous and metamorphic rocks, mainly granites, gneisses, or schists. The mineralization in Western Galicia can be classified into two main types associated with different petrographic units. The first type is iron and copper sulphide mineralization, which is linked to the mafic complex. The second type is lithium, tin, and tungsten mineralization, which is associated with granites[13]. These elements are present in the placer deposits found in the Rias Baixas region and are the target of the study.

2. DATA AND METHODS

2.1 Data

At this stage, Sentinel-1 data was only downloaded for the Aramo region due (i) higher outcrop exposition in Aramo favoring lithological mapping approaches; (ii) possible structural controls of the mineralization in Aramo; and (iii) low exposition of placers in the Rias Baixas area. The Sentinel-1A image was obtained with the Interferometric Wide (IW) swath acquisition mode in descending orbit on 7 January 2023. A Level-1 Ground Range Detected (GRD) high-resolution was obtained.

Regarding Sentinel-2 satellite data, images with low cloud and water coverage were selected. Moreover, high vegetation coverage was avoided for the inland study area, since the vegetation coverage is not so relevant on the coastal areas. The optical data for the Aramo area was acquired by Sentinel-2B on 28 June 2023 with less than 1% of snow and water coverage, but with a vegetation coverage of 84%. A Level-2A product was downloaded already with surface reflectance values, and associated cloud, vegetation, ice, snow, and water masks. For the Rias Baixas, a Level-2A product of a Sentinel-2A image acquired on 16 February 2023 was used with less than 1% cloud coverage, around 15% of water coverage a less than 64% vegetation coverage.

2.2 Pre-processing

All pre-processing was done using the European Spatial Agency (ESA)'s Sentinel Application Platform (SNAP).

A typical synthetic aperture radar (SAR) pre-processing workflow was employed through the Sentinel-1 Toolbox (S1TB)[14], as described in detail in previous works[5]: (i) cropping (to match the coordinate extent of Sentinel-2 images in each study area); (ii) orbit correction (using the provided orbit file to obtain a more accurate satellite position and velocity information); (iii) thermal noise removal (through a bi-linear interpolation); (iv) radiometric calibration (the pixel digital numbers (DNs) were converted into radiometrically calibrated backscatter values); (v) texture analysis through the Grey Level Co-occurrence Matrix (GLCM) method[15]; (vi) speckle noise reduction (using a Lee sigma spatial filter[16]); (vii) terrain correction (using the Range Doppler Terrain Correction method[17]) and automatic geometric resampling to 10 m spatial resolution; (viii) final geographic trimming.

Since a higher processing level product was used, limited pre-processing was necessary for Sentinel-2. The bands were resampled to 10 m spatial resolution by upsampling the bands provided with 20 m and 60 m Ground Sample Distance (GSD) through the Nearest Neighbor method. For the Aramo area, since the vegetation mask provided with the Level 2A product covered most of the outcrops, new vegetation masks were produced. First, the normalized difference vegetation index (NDVI)[18] was applied. Then, different NDVI value thresholds were tested to compute the vegetation mask from 0.25 to 0.50. The threshold that allowed to generate the mask that better matched with the natural colors RGB combination was selected (in this case, 0.43).

2.3 Processing

Known combinations and algorithms from the literature were employed to detect and map areas of hydrothermal alteration in both study areas and to try to detect placer minerals in Rias Baixas. In some cases, trial-and-error was also used to select the input bands and test self-proposed combinations. Specifically, published reference spectra of minerals of interest were used to select the input Sentinel-2 bands for the application of the image processing algorithms.

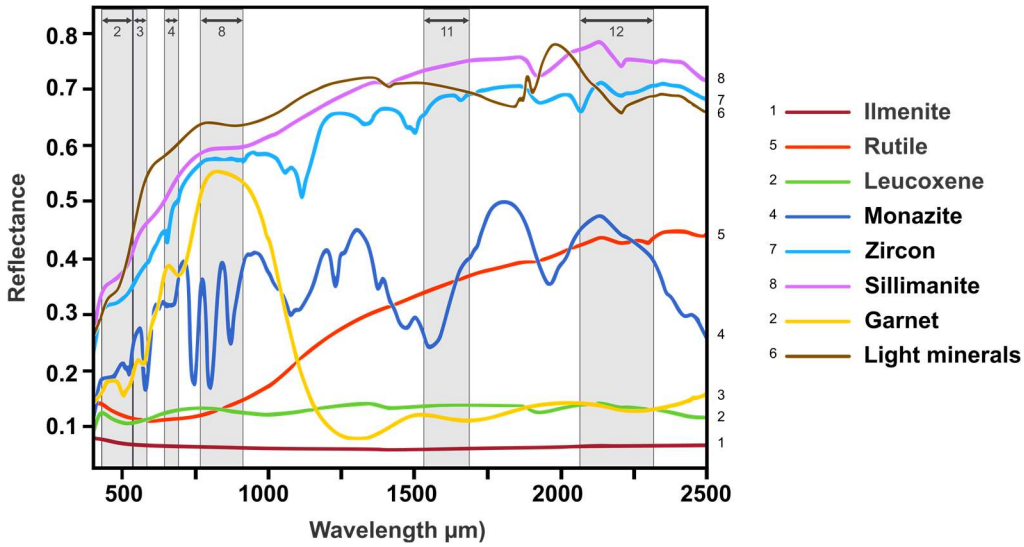

Figure 2. Superposition of the Sentinel-2 bands over the reference spectra of common beach minerals to select the input bands for the image processing on Rias Baixas. Adapted from: Rejith, et al. [19].

As a first assessment, RGB combinations allow getting an overview of the spectral classes of the images. Tested combinations are listed in Table 1.

Table 1. Tested RGB combinations on both case studies for Sentinel-1 and Sentinel-2 images.

Data type	Input Bands	Target	Case study
Sentinel-1	VH Contrast-VH Dissimilarity-VV Contrast	Lithological discrimination	Aramo
	VH Contrast-VH GLCM Mean-VV Contrast		
	VH Homogeneity-VV Homogeneity-VH Contrast		
	PC1-PC2-PC3*		
Sentinel-2	2-8-12[20]	Iron oxides and clay minerals	Aramo, Rias Baixas
	8-11-12[6]	Hydrothermally altered rocks	
	8-12-3[21]	Hydrothermally altered rocks	
	11-8-12[20]	Iron oxides and clay minerals	
	11-4-12[22]	Lithological contrasts	
	8-11-2[23]	Healthy vegetation	
	8-11-4[23]	Land/Water	
	12-8-4[23]	Lithological discrimination	
	9-8-3	Lithological discrimination	
	5-6-11	Lithological discrimination	
	11/12-4/3-8/11[21]	Abrams' ratio: iron oxides/clays	Rias Baixas

* PC – principal component; see Table 3

The band ratio method (Table 2) was used to map specific minerals related to hydrothermal alteration. Other band ratios were tested.

Table 2. Tested band ratios based on Sentinel-2 data for the two case studies.

Data type	Input Bands	Target	Case study
Sentinel-2	4/3[24-26]	Ferric iron/oxides	Aramo, Rias Baixas
	(12/8)+(3/4)[25, 26]	Ferrous Iron	
	12/11[25, 26]	Ferrous silicates (Biotite, chloride, amphibole)	
	11/8[26, 27]	Ferric oxides	
	11/12[25, 26]	Laterite/Silicate alteration	
	11/4[25, 26]	Gossan	
	8/12	—	
	12/5	—	
	4/12	—	
	6/12	—	
	8/3	—	
	8/12	Garnet	Rias Baixas
	12/8	Rutile, Monazite	
	12/3	Monazite	

Selective PCA was adopted in this study to directly target hydrothermal alteration minerals. This approach requires the user to select the most appropriate bands considering the spectral behavior of the desired targets. Afterwards, PCA is applied on either a two-band or a four-band subset (Table 3).

Table 3. PCA band subsets employed with Sentinel-1 and Sentinel-2 data in the case study areas.

Data type	Input Bands	Target	Case study
Sentinel-1	All GLCM co-occurrence indices on VV and VH polarizations (Contrast, Dissimilarity, Homogeneity, Angular Second Moment, Maximum Probability, Entropy, GLCM Mean, GLCM Variance, GLCM Correlation)	Lithological mapping	Aramo
Sentinel-2	2, 4[24, 28]	Ferric iron	Aramo, Rias Baixas
	2, 4, 8, 11[24, 29]		
	11, 12[24, 28]	Hydroxyl minerals	
	2, 8, 11, 12[24, 29]		

The unsupervised classification was performed using the K-means clustering algorithm with 20 iterations and the same random seed, but varying the number of clusters (4, 8, 10, 14) and the source bands as shown in Table 4.

Table 4. Input parameters used for unsupervised classification of Sentinel-1 and Sentinel-2 data for both study areas.

Data type	Input Bands	No. clusters	Case study
Sentinel-1	PC bands	14	Aramo, Rias Baixas
		8	
	All GLCM co-occurrence indices on VV and VH polarizations	14	
		8	
Sentinel-2	2, 3, 4	14	
	2, 3, 4, 8		
	2, 3, 4, 11, 12		
	2, 3, 4, 8, 11, 12	14	
		8	
	2, 3, 4, 5, 6, 7, 8, 11, 12	14	
		8	
	1, 2, 3, 4, 5, 6, 7, 8, 8A, 11, 12	14	
		4	
		8	
		10	

3. RESULTS AND DISCUSSION

This section presents and discusses the most meaningful results obtained with the employed image processing techniques for each case study area.

3.1 Aramo

As a result of the pre-processing, textural analysis of Sentinel-1 SAR data resulted in 10 different co-occurrence indices that provide information on contrast features (contrast, dissimilarity, and homogeneity), orderliness features (angular second moment, maximum probability, energy, and entropy), and statistics features (mean, variance, and correlation) on each polarization (VV and VH), resulting in 20 indices. The direct interpretation of such indices is not straightforward, so by trial and error, the indices were combined in RGB combinations. However, even the produced RGB combinations can be difficult to interpret due to shadow effects on mountainous regions. In general, it is possible to identify well (i) the outlines of the alluvial fans in the South of the area, (ii) urban agglomerates within these alluvial fans (city of León), (iii) the contact between the alluvial fans (Douro Basin) and the Fold and Nappe geological province[30] as well as the boundary between the Fold and Nappe geological and the Asturian Central Coal Basin to the North where the Aramo mine is located.

To reduce the redundancy and data dimension, PCA was applied to the 20 co-occurrence indices. Both the resulting principal components (PCs) and the original indices served as inputs for unsupervised classification, respectively (Figure 3). Similar to the RGB combinations, K-means clustering maps also allowed identifying (i) urban areas (not shown in Figure 3), (ii) the outlines of the alluvial fans, and (iii) the contacts between the Douro Basin – Fold and Nappe geological province – Asturian Central Coal Basin. Overall, the unsupervised classification approach based on 14 clusters (Figure 3-b and -d) discriminated water bodies such as dams from other within-scene elements, but the higher number of classes hinders the identification of geological contacts. The ideal number of clusters was found to be eight for both input datasets (Figure 3-a and -c). On the other hand, a choice of 14 clusters allows a quick recognizance of zones where certain lithological homogeneity can be expected. Folding patterns, for example, are more evident in Figure 3-d. When more clusters are used there is a different performance depending on the choice of different input bands, with the K-means algorithm forming more concise clusters with all GLCM co-occurrence indices on VV and VH polarizations bands.

Looking at the close-up views of the Aramo mine (Figure 3-a1 to -d1), the NE border of the plateau is well-marked on all maps. Patches of vegetation are identified in light green (Figure 3-d1) and light purple (Figure 3-a1) while all vegetated

areas are grouped in the same pale-green cluster in Figure 3-c1. Outcrop areas are subdivided into several clusters displaying similar patterns in all maps. Additional studies coupled with field surveys are needed to understand why different clusters are identified and what is the correspondence on the ground.

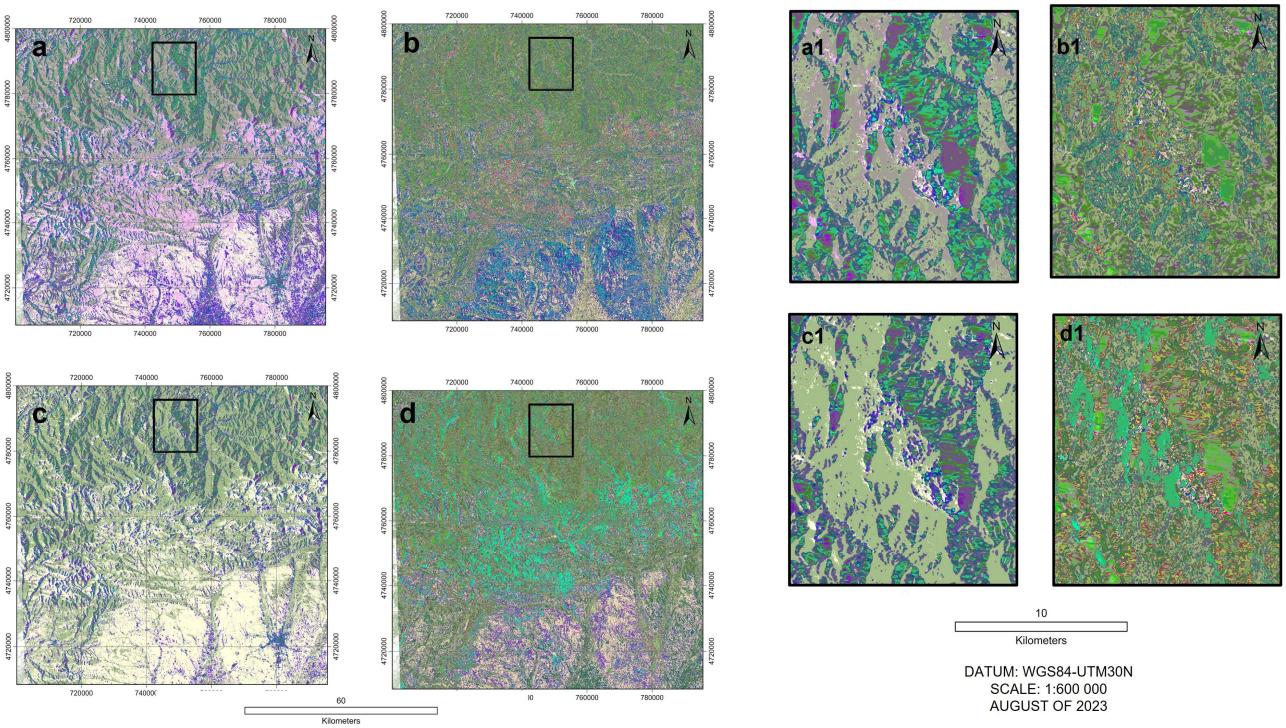

Figure 3. Sentinel-1 unsupervised classification using the K-means clustering algorithm: a) eight initial clusters with all GLCM co-occurrence indices as inputs; b) 14 clusters with all GLCM indices; c) eight clusters with the PCs as input bands; and d) 14 initial clusters with the PCs as inputs. The visualization is improved when fewer classes are created.

Regarding the results obtained with Sentinel-2, it was expected that the optical data would be impacted mainly by vegetation coverage. This can be seen in Figure 4 where a vegetation mask is overlayed in green and pale green (Figure 4-a, -e, -f) as well as in brown to brownish orange colors (Figure 4-b, -c, -d). The outer shape of the alluvial fans is evident, as well as the distinction between different types of vegetation coverage/agricultural fields within the fans (Figure 4-b, -c, -d). The folding patterns are evident in Figure 4-d. This RGB combination is specially designed for lithological contrasts[22]. However, Figures 4-b and -c also allow to identify these patterns. The boundaries between the Douro Basin and the Fold and Nape geological province as well as between the latter and the Asturian Central Coal Basin are more Defined in Figure 4-a, -e, and -f. RGB combination 5-6-11 provides a similar distinction between iron oxides and clay minerals as Figure 4-a. According to the literature[6, 21], RGB combination 8-11-12 (Figure 4-b) should highlight hydrothermally altered rocks in yellow color while RGB combination 8-12-3 (Figure 4-c) should highlight such alterations in deep green and blue colors. However, when looking at the close-up views of the Aramo Plateau (Figure 4-a1 to-f1), it is clear that these combinations fail in the identification of hydrothermal alteration areas. In Figure 4-b1, some white to yellowish pixels are identified, while in Figure 4-c1, the deep green color to the SW corner represents an area possibly affected by wildfires. When looking at a regional scale, the RGB combination in Figure 4-c for hydrothermally altered rocks seems to perform better than the combination tested in Figure 4-b, with some outcrops south of the Aramo area highlighted in baby blue.

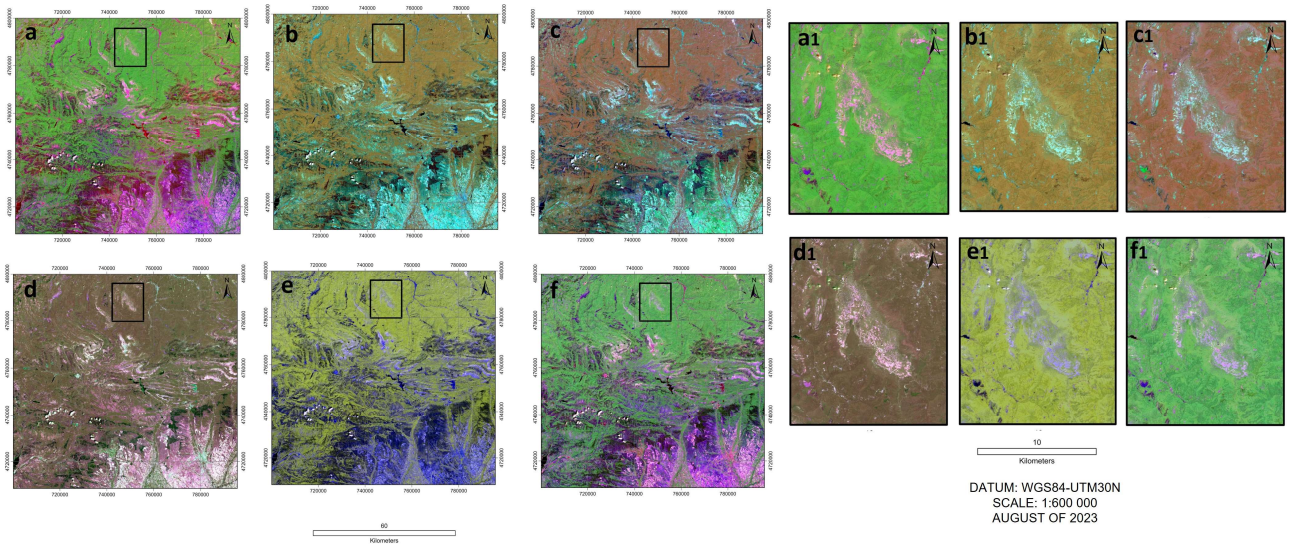

Figure 4. Different RGB combinations in the Aramo area using Sentinel-2, and detail of the Aramo Plateau for each image: a) RGB 2-8-12 to map iron oxides and clay minerals; b) RGB 8-11-12 to identify hydrothermally altered rocks; c) RGB 8-12-3 for hydrothermally altered rocks; d) RGB 11-4-12 to highlight lithological contrasts; e) RGB 9-8-3; and f) RGB 5-6-11.

To enhance the results of the band ratio method, a density slice technique was used to attribute a color palette according to the images' histograms. Thus, cold colors represent low ratio values, while hot colors represent high pixel values and therefore the areas where the target minerals should occur. The results are presented in Figure 5, where the band ratios are overlayed by a vegetation mask in green color. This vegetation mask is crucial since most of the high ratio pixels correspond to areas where there is some type of vegetation (trees in the mountains in the North; trees and shrubs along the water lines; and agricultural fields in the alluvial fans to the South).

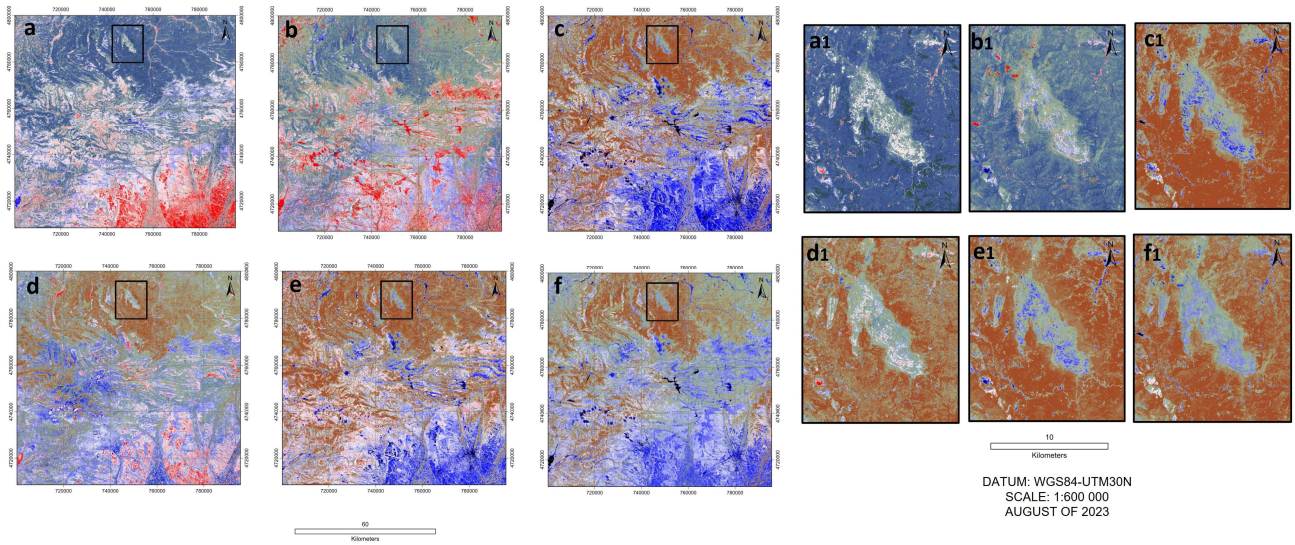

Figure 5. Different band ratios for Sentine-2 data in the Aramo area: a) B4/B3 targeting ferric iron/oxides; b) B4/B12; c) B8/B12; d) (B12/B8)+(B3/B4) targeting ferrous iron; e) B11/B12 targeting laterite/silicate alteration; and f) B11/B4 targeting gossan formation.

Band ratio 4/3 (Figure 5-a) maps iron oxides in red pixels in outcrops South of the Aramo Plateau as well as along the Fold and Nape geological province. When looking at the close-up view (Figure 5-a1), there are some small regions within the plateau that present iron oxides. Ferrous iron is detected in some outcrops West of the Aramo Plateau and along the Fold and Nape geological province (Figure 5-d). Small regions within the Adamo Plateau also point to the presence of ferrous

oxides (Figure 5-d1). Band ratio 11/12 (Figure 5-e) highlights silica alteration in a mountainous outcrop West of the Aramo Plateau. The self-proposed band ratio in Figure 5-c shows similarities in the Aramo Plateau with the band combination in Figure 5-e, which targets laterite and/or silicate alteration. Lastly, the self-proposed band ratio in Figure 5-b highlights different zones in the Aramo Plateau that are worth further analysis in the field.

As aforementioned, PCA was applied in selected subsets of bands to identify iron-rich minerals and hydroxyl-bearing minerals such as micas and clays. The same density slice technique was employed and the results are presented in Figure 6. Again, a vegetation mask was overlaid over the resultant PCs. PCA is more effective in target detection with fewer interest areas delimited. However, there are some false positives with some clouds in Figure 6-a, -b, and -d highlighted in red color. Overall, the four band subsets result in larger areas highlighting the alteration minerals (Figure 6-b, -d). Adding more bands doesn't seem to add significant improvement to the analysis in iron oxide detection. However, to target hydroxyl minerals, the addition of more bands brings a significant improvement when compared with the two-band subset. Despite this, the presence of hydroxyl-bearing minerals within the plateau seems very limited since there are no high pixel values highlighted in red color (Figure 6-c1, -d1).

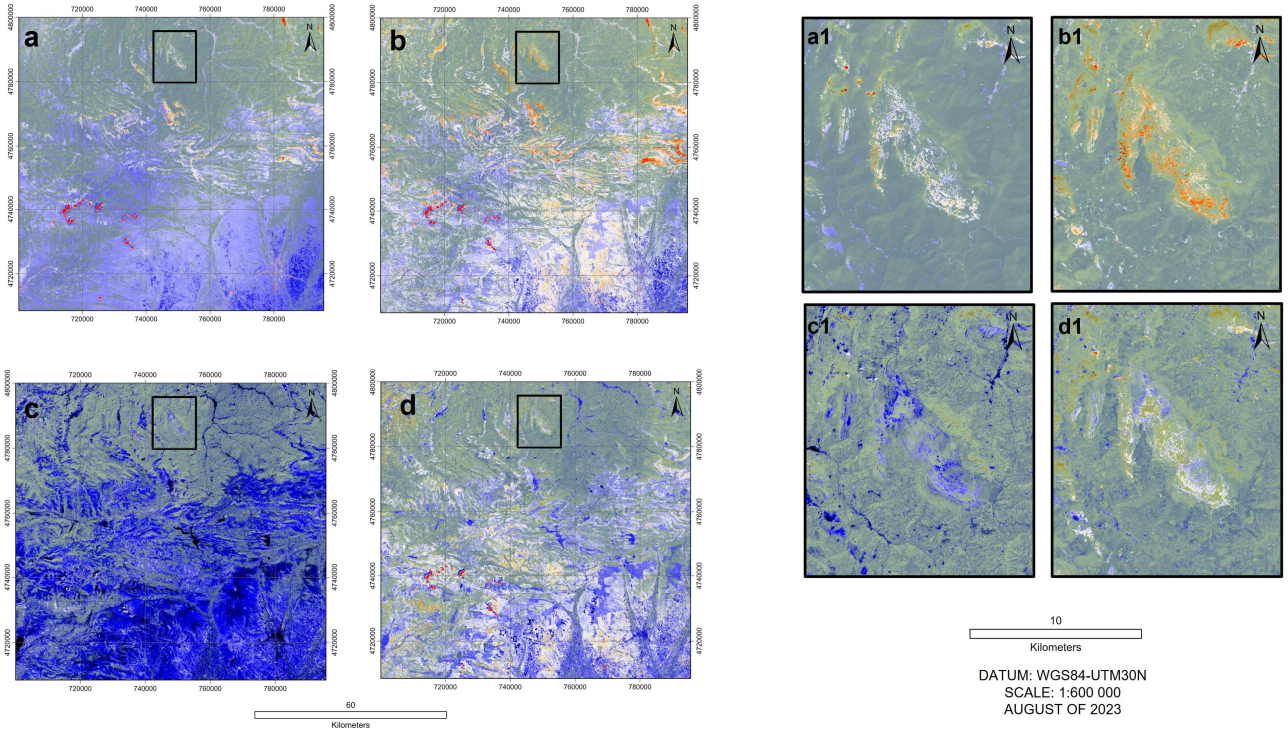

Figure 6. PCA in the Aramo mine zone: using the bands 2,4 (a) and 2,4,8,11 (b), respectively, targeting ferric oxides; using the bands 11,12 (c) and 2,8,11,12 (d), respectively, to target hydroxyl minerals.

The results of the unsupervised classification attempt are presented in Figure 7. Vegetation masks appear in gray/pale gray and green colors. The folding patterns are visible in all the classification results. In general, when using 14 initial clusters, there is a better discrimination of the alluvial fans and the different land cover classes within the fans (Figure 7-a, -c). The lithological boundaries are easier to identify when the initial number of clusters is smaller (eight; Figure 7-b, -d). In the Aramo Plateau (Figure 7-a1 to -d1), the clustering results are more consistent when only eight initial clusters are used with the different input bands selected. Therefore, the clusters identified are worth further investigation in the field.

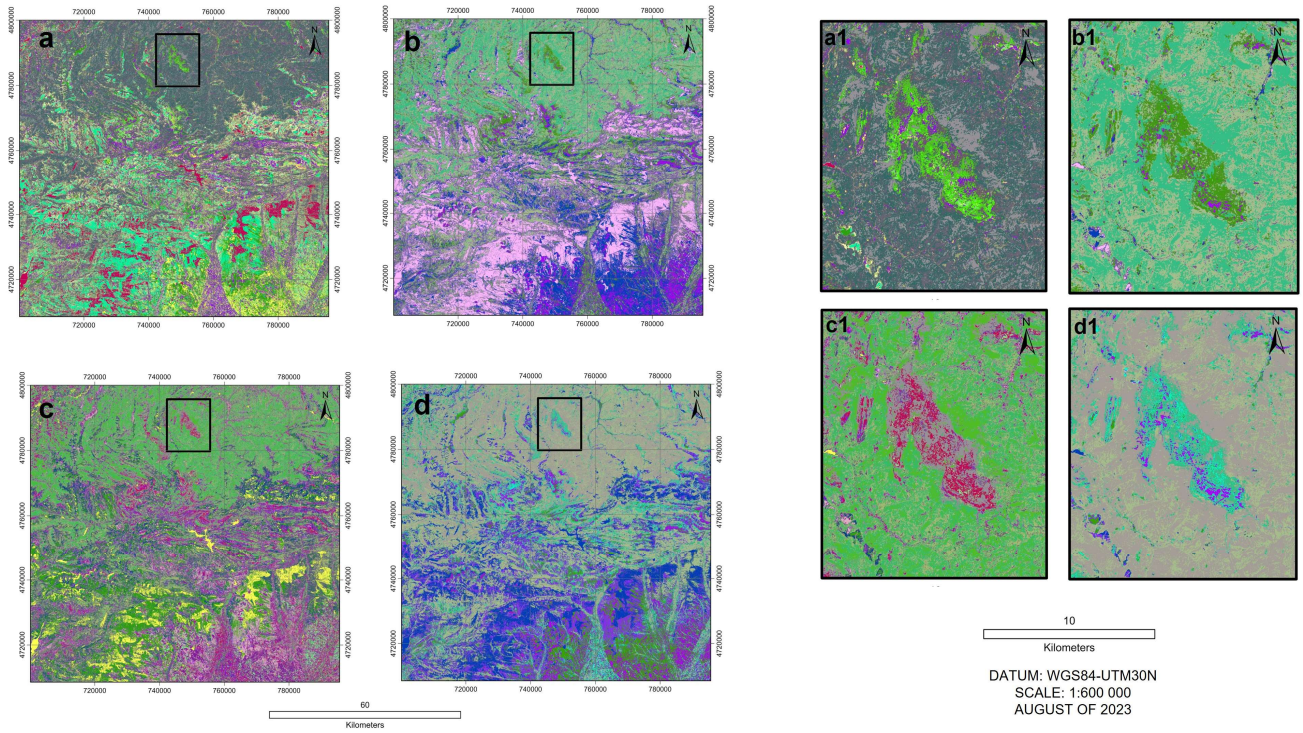

Figure 7. Sentinel-2 unsupervised classification using the K-means clustering algorithm in Aramo: a) with 14 clusters and the following input bands B2, B3, B4, B5, B6, B7, B8, B11, B12; b) with eight clusters and bands B2, B3, B4, B5, B6, B7, B8, B11, B12 as inputs; c) with 14 clusters and input bands B2, B3, B4, B8, B11, B12; and d) with eight clusters and the following bands B2, B3, B4, B8, B11, B12 as inputs. Similar results are obtained for the different input bands with the same number of clusters.

The low Sentinel mapping capabilities of hydroxyl minerals in the Aramo area would be expected since, in this region, the hydrothermal alteration related to the Co-Cu-Ni deposits results in dolomitization, while clay formation is not well documented and studied for this area and deposit type. Thus, further studies are needed to understand if in fact there is some clay mineral formation related to the epigenetic deposits. Regarding, the potential to map dolomization areas, there is a carbonate absorption feature at around 2300 nm that falls within the same Sentine-2 band (B12) of the hydroxyl absorption at 2200 nm. Therefore, it is necessary a higher spectral resolution in the SWIR region to map this type of alteration.

In the future, S34I will (i) assess the usefulness of supervised classification algorithms; (ii) test hyperspectral data and very high-resolution data such as PRISMA and Worldview-3, respectively; and (iii) characterize in detail the hydrothermal alteration associated with the epithermal Co-Cu-Ni deposits. Moreover, to fully exploit radar data, Sentinel-1 will be used to perform lineament extraction and structural mapping (i.e., structural controls of the mineralization) as done in previous works[31, 32]. The integration of Sentinel-1 and Sentinel-2 could be considered using AI, specifically machine learning algorithms.

3.2 Rias Baixas

When looking at the RGB combinations for Rias Baixas (Figure 8), the vegetation appears in green colors in Figures 8-a and -b, in orange in Figures 8-c and -d, and in red color in Figures 8-e and -f. Some combinations highlight the impact of the waves against the shoreline as well as the boats' trajectories (Figure 8-a, -c, -e, -f). Overall, known beaches where placers occur appear in bright white in all RGB combinations. Muscle farms in the region can be seen in some combinations, for example in Figure 8-a1 and -f1.

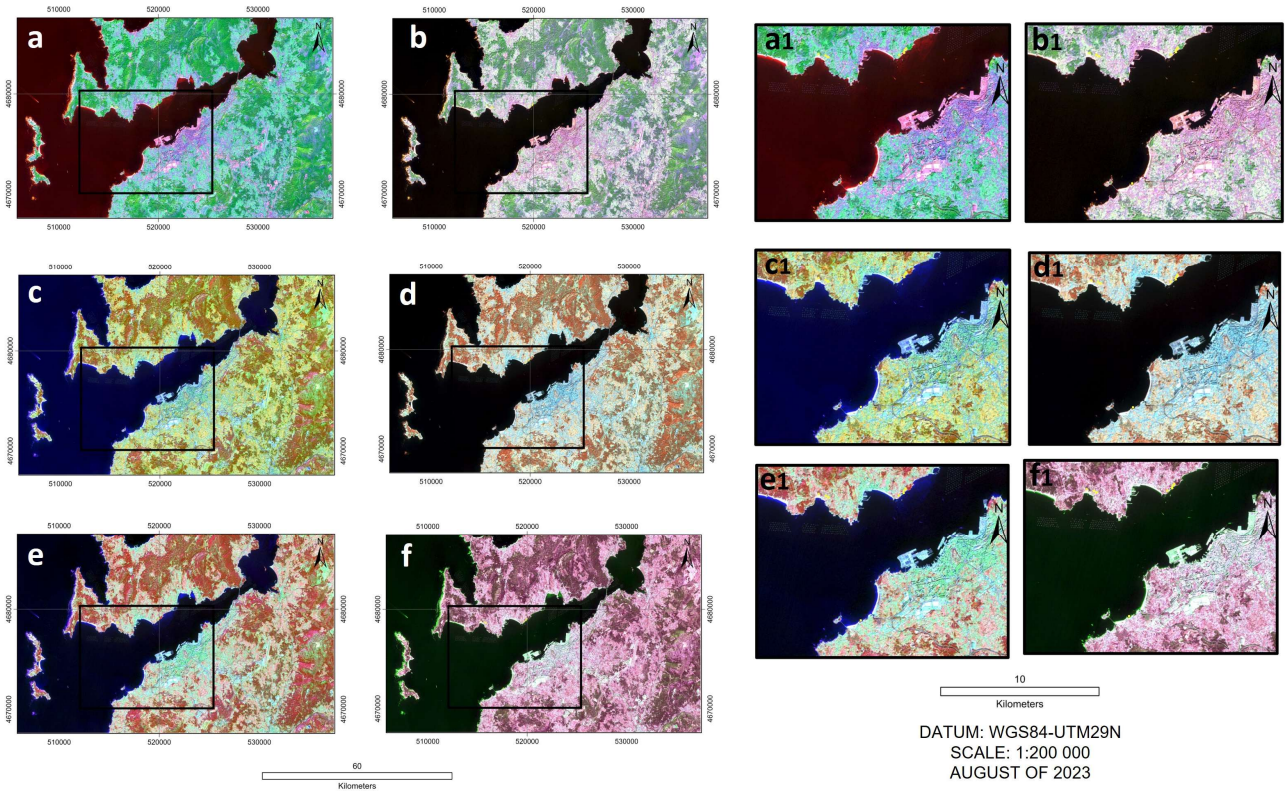

Figure 8. Different RGB compositions using Sentinel-2 in the Rias Baixas area: a) RGB 2-8-12; b) RGB 5-6-11; c) RGB 8-11-2; d) RGB 8-11-12; e) RGB 8-B12-B3; f) RGB 11-4-12.

Figure 9 shows the band ratios with a vegetation mask overlayed on top. The ferric oxides ratio (Figure 9-a) highlights mainly pixels within urban areas. The self-proposed band ratio 8/12 to identify garnets (Figure 9-b) shows potential as some pixels within the beaches appear in red, but there is some influence from the breaking waves. Band ratio 11/12 for silicate alteration mapping (Figure 9-c) shows, in some places, red color along the shoreline and on land, but the false positives are once again mainly related to the breaking waves. The ferrous iron ratio (Figure 9-f) highlights underwater areas near the shore that probably correspond to low-depth zones. Muscle farms are highlighted by all ratios except for the silicate alteration one (Figure 9-c).

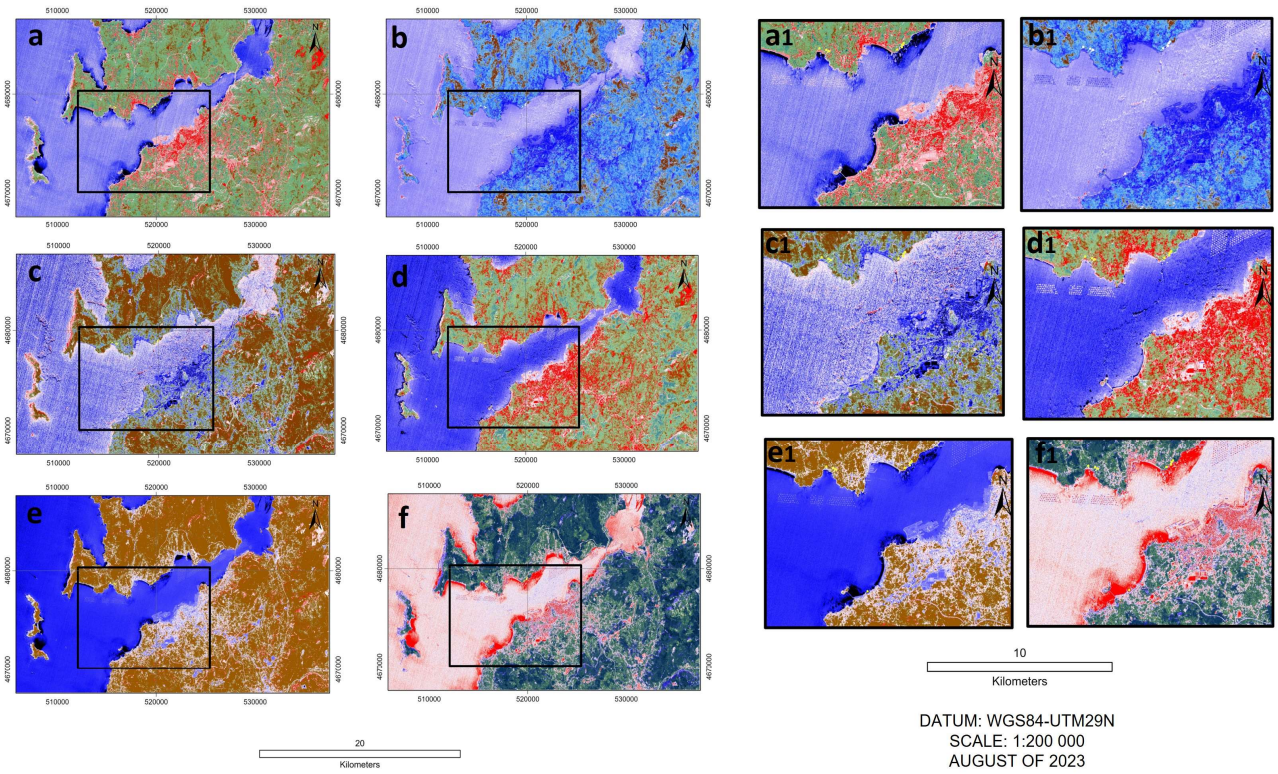

Figure 9. Sentinel-2 band ratios for Rias Baixas: a) B4/B3; b) B8/B12; c) B11/B12; d) B12/B5; e) B8/B3; and f) (B12/B8)+(B3/B4).

The PCA results based on the four-band subset are presented in Figure 10. As can be seen, hydroxyl-bearing minerals are not identified in the region (Figure 10-a). Oppositely, iron oxides (Figure 10-b) are mapped with different degrees of confidence in the beaches, showing a much better performance than the band ratio technique.

The unsupervised classification results are shown in Figure 11. Using the red edge band produces very similar outputs to when they are not used as inputs. Increasing the number of clusters in both band combinations allows to visualize differences in the interest zone of Rias Baixas (Figure 11-b1 and -d1). When using 14 clusters, three different spectral classes are identified within the water, worth exploring in detail.

In summary, very-high spatial resolution seems to be critical to map CRM on coastal areas due to the small exposition and particle size of placer minerals. Future studies within the S34I project could include: (i) analysis of the potential of Sentinel-1 in coastal areas; (ii) Sentinel-2 bathymetry studies to get a better overview of the seafloor; and (iii) the acquisition of in situ samples to study the spectral properties of the placer minerals. The obtention of reference spectra will be fundamental to perfecting the image processing algorithms. For that, not only laboratory measurements will be conducted but S34I will deploy a new and innovative Underwater Hyperspectral Imaging (UHI) system to build a spectral library for ground-truthing and correlation with satellite data.

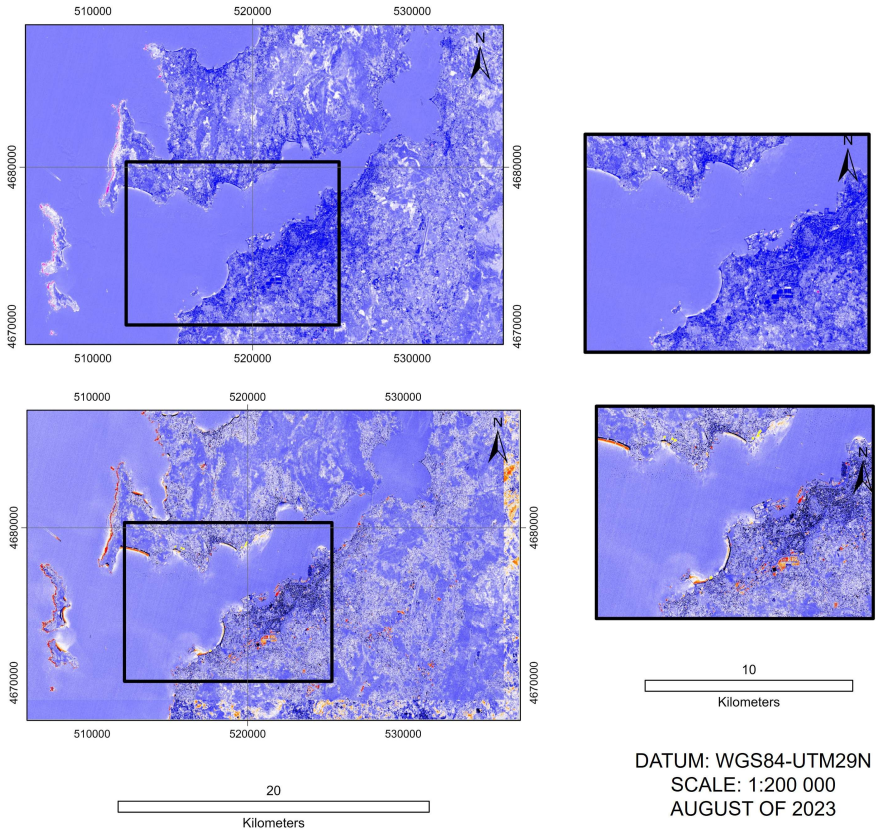

Figure 10. PCA based on the four band subsets in the Rias Baixas: a) PC4 targeting hydroxides components; b) PC4 targeting iron oxides.

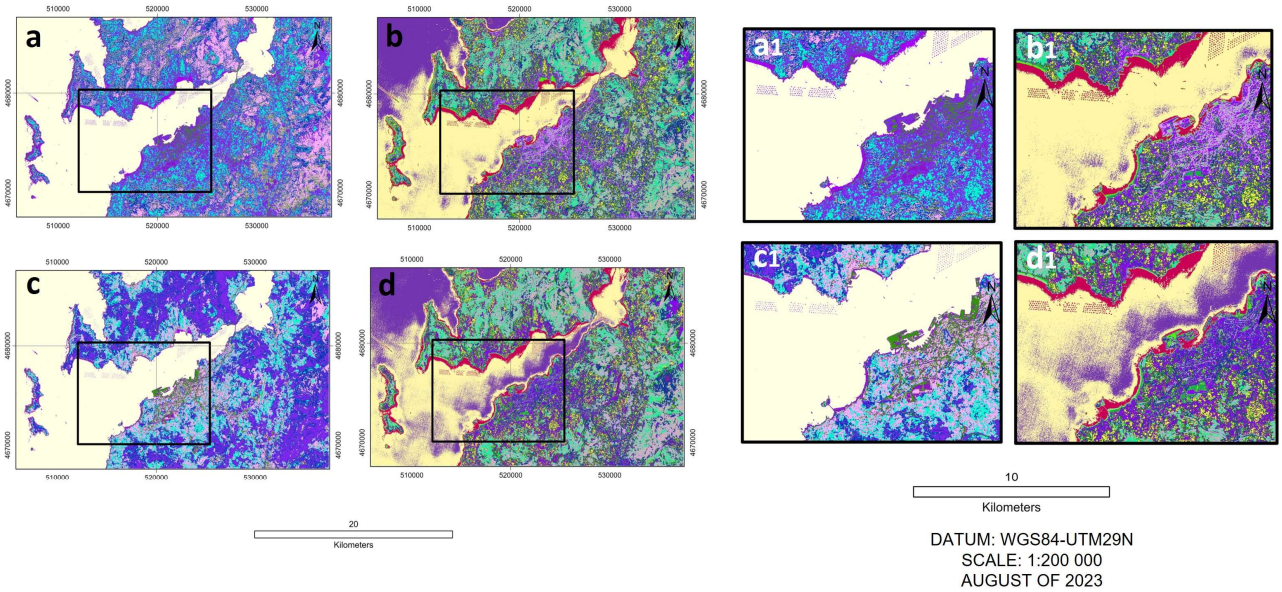

Figure 11. Sentinel-2 unsupervised classification using the K-means clustering algorithm in the Rias Baixas; a) with eight clusters and the following input bands B2, B3, B4, B5, B6, B7, B8, B11, B12; b) with 14 cluster and bands B2, B3, B4, B5, B6, B7, B8, B11, B12 as inputs; c) with eight clusters and input bands B2, B3, B4, B8, B11, B12; and d) with 14 clusters and the following bands B2, B3, B4, B8, B11, B12 as inputs.

4. CONCLUSIONS

This study aimed to leverage the capabilities of Copernicus Sentinel data to identify potential areas for CRM deposits, focusing on Co in the Aramo area and placers deposits in Rias Baixas. The suitability of Sentinel-1 and Sentinel-2 data was evaluated. The results demonstrated the potential of Sentinel data in detecting lithological features, geological contacts, and hydrothermal alteration zones in both study areas. Optical data was in general more informative, but radar data can be very useful for lithological contact mapping. However, the benefits of integrating Sentinel-1 and Sentinel-2 data still need to be evaluated. The performance of classical image processing techniques for mapping Co-related hydrothermal alterations and placers was also compared. Among the techniques, PCA was the most effective followed by band ratios. The clusters generated through unsupervised classification need to be verified in the field to assess the possible contributions of such an approach. Moreover, self-proposed algorithms to detect placer minerals should be further investigated. However, the accurate identification of hydrothermal alterations and placers presented challenges, indicating the need for further research and ground validation. This can be achieved with supervised classification algorithms and hyperspectral/very-high spatial resolution data. Future studies within the S34I project will focus on refining image processing techniques, exploring new datasets, acquiring in-situ samples and collecting data through UHI to improve the accuracy and reliability of CRM mapping. Ultimately, these advancements hold great promise for supporting sustainable resource management and addressing the growing demands in the battery market and other critical industries reliant on CRM.

ACKNOWLEDGMENTS

This study is funded by European Union under grant agreement no. 101091616, project S34I – SECURE AND SUSTAINABLE SUPPLY OF RAW MATERIALS FOR EU INDUSTRY. The S34I project is coordinated by Ana C. Teodoro. The Portuguese partners also acknowledge the support provided by Portuguese National Funds through the FCT – Fundação para a Ciência e a Tecnologia, I.P. (Portugal) projects UIDB/04683/2020 and UIDP/04683/2020 (Institute of Earth Sciences).

REFERENCES

[1] Benchmark Minerals, "Battery powered: 20 years of lithium demand," 2023, <https://source.benchmarkminerals.com/article/battery-powered-20-years-of-lithium-demand> (3 August 2020)

[2] J. Cardoso-Fernandes, A. C. Teodoro, A. Lima, M. Perrotta, and E. Roda-Robles, "Detecting Lithium (Li) Mineralizations from Space: Current Research and Future Perspectives," Applied Sciences, 10(5), 1785 (2020); doi: 10.3390/app10051785.

[3] F. D. van der Meer, H. M. A. van der Werff, F. J. A. van Ruitenbeek, C. A. Hecker, W. H. Bakker, M. F. Noomen, M. van der Meijde, E. J. M. Carranza, J. B. d. Smeth, and T. Woldai, "Multi- and hyperspectral geologic remote sensing: A review," International Journal of Applied Earth Observation and Geoinformation, 14(1), 112-128 (2012); doi: 10.1016/j.jag.2011.08.002.

[4] M. Köhler, D. Hanelli, S. Schaefer, A. Barth, A. Knobloch, P. Hielscher, J. Cardoso-Fernandes, A. Lima, and A. C. Teodoro, "Lithium Potential Mapping Using Artificial Neural Networks: A Case Study from Central Portugal," Minerals, 11(10), 1046 (2021); doi: 10.3390/min11101046.

[5] J. Cardoso-Fernandes, A. C. Teodoro, A. Lima, J. Menuge, M. Brönner, and R. Steiner, "Sentinel-1 and ALOS data for lineament extraction: a comparative study." 12268 (2022); doi: https://doi.org/10.1117/12.2636117.

[6] A. B. Pour, M. Hashim, and M. Marghany, "Exploration of gold mineralization in a tropical region using Earth Observing-1 (EO1) and JERS-1 SAR data: a case study from Bau gold field, Sarawak, Malaysia," Arabian Journal of Geosciences, 7(6), 2393-2406 (2014); doi: 10.1007/s12517-013-0969-3.

[7] S. Beato Bergua, M. Á. Poblete Piedrabuena, C. Rodríguez Pérez, and J. L. Marino Alfonso, "Geomorphology of the Sierra del Aramo (Asturian Central Massif, Cantabrian Mountains, NW Spain)," Journal of Maps, 15(2), 590-600 (2019); doi: 10.1080/17445647.2019.1646675.

[8] A. Paniagua, J. Loredo, and J. Garcia Iglesias, "Epithermal (Cu-Co-Ni) mineralization in the Aramo mine (Cantabrian mountains, Spain): correlation between paragenetic and fluid inclusion data." https://www.persee.fr/doc/bulmi_0180-9210_1988_act_111_3_8059.

[9] C. Aramburu, F. Bastida, and M. Arbizu, [Geología de Asturias], Ediciones Trea, Gijón, Spain, 314 (1995).

[10] M. G. Claverol, and C. L. Cabal, [Recursos del subsuelo de Asturias], Universidad de Oviedo, Servicio de Publicaciones, Oviedo, Spain, 392 (1993).
[11] M. Iglésias, M. L. Ribeiro, and A. Ribeiro, "La interpretación aloctonista de la estructura del noroeste peninsular", [Libro jubilar J.M. Rios], J. A. Comba, Ed., Instituto Geologico y Minero de España, Madrid, Spain, 459–467 (1983).
[12] G. Méndez, and F. Vilas, "Geological antecedents of the Rias Baixas (Galicia, northwest Iberian Peninsula)," Journal of Marine Systems, 54(1), 195-207 (2005); doi: https://doi.org/10.1016/j.jmarsys.2004.07.012.
[13] A. Koschinsky, M. Van Gerven, and P. Halbach, "First investigations of massive ferromanganese crusts in the NE Atlantic in comparison with hydrogenetic pacific occurrences," Marine Georesources & Geotechnology, 13(4), 375-391 (1995); doi: 10.1080/10641199509388294.
[14] "SNAP," <https://step.esa.int/main/toolboxes/snap/> (20 April 2020)
[15] R. M. Haralick, K. Shanmugam, and I. Dinstein, "Textural Features for Image Classification," IEEE Transactions on Systems, Man, and Cybernetics, SMC-3(6), 610-621 (1973); doi: 10.1109/TSMC.1973.4309314.
[16] J. S. Lee, and E. Pottier, [Polarimetric SAR Radar Imaging: From Basic to Applications], CRC Press, Taylor & Francis Group, Boca Raton, London, New York (2009).
[17] D. Small, and A. Schubert, [Guide to ASAR Geocoding], University of Zurich, Zurich, Switzerland, (2008); doi, https://www.geo.uzh.ch/microsite/rsl-documents/research/publications/other-sci-communications/2008_RSL-ASAR-GC-AD-v101-0335607552/2008_RSL-ASAR-GC-AD-v101.pdf.
[18] J. W. Rouse, R. H. Haas, J. A. Schell, and D. W. Deering, "Monitoring vegetation systems in the Great Plains with ERTS." 1, 48-62 (1974).
[19] R. G. Rejith, M. Sundararajan, L. Gnanappazham, and V. J. Loveson, "Satellite-based spectral mapping (ASTER and Landsat data) of mineralogical signatures of beach sediments: a precursor insight," Geocarto International, 37(9), 2580-2603 (2022); doi: 10.1080/10106049.2020.1750061.
[20] A. Ali, and A. Pour, "Lithological mapping and hydrothermal alteration using Landsat 8 data: a case study in ariab mining district, red sea hills, Sudan," International Journal of Basic and Applied Sciences, 3(3), (2014); doi: 10.14419/ijbas.v3i3.2821.
[21] B. Mia, and Y. Fujimitsu, "Mapping hydrothermal altered mineral deposits using Landsat 7 ETM+ image in and around Kuju volcano, Kyushu, Japan," Journal of Earth System Science, 121(4), 1049-1057 (2012); doi: 10.1007/s12040-012-0211-9.
[22] M. W. Mwaniki, M. S. Moeller, and G. Schellmann, "A comparison of Landsat 8 (OLI) and Landsat 7 (ETM+) in mapping geology and visualising lineaments: A case study of central region Kenya," ISPRS - International Archives of the Photogrammetry, Remote Sensing and Spatial Information Sciences, XL-7/W3, 897-903 (2015); doi: 10.5194/isprsarchives-XL-7-W3-897-2015.
[23] European Space Agency (ESA), "SNAP Help documentation," (1 August 2023).
[24] J. Cardoso-Fernandes, A. C. Teodoro, and A. Lima, "Remote sensing data in lithium (Li) exploration: A new approach for the detection of Li-bearing pegmatites," International Journal of Applied Earth Observation and Geoinformation, 76, 10-25 (2019); doi: https://doi.org/10.1016/j.jag.2018.11.001.
[25] F. D. van der Meer, H. M. A. van der Werff, and F. J. A. van Ruitenbeek, "Potential of ESA's Sentinel-2 for geological applications," Remote Sensing of Environment, 148, 124-133 (2014); doi: 10.1016/j.rse.2014.03.022.
[26] A. Kalinowski, and S. Oliver, [ASTER Mineral Index Processing Manual], Geoscience Australia, (2004).
[27] C. Hecker, M. v. der Meijde, and F. D. van der Meer, "Thermal infrared spectroscopy on feldspars — Successes, limitations and their implications for remote sensing," Earth-Science Reviews, 103(1), 60-70 (2010); doi: https://doi.org/10.1016/j.earscirev.2010.07.005.
[28] P. S. Chavez Jr, and A. Y. Kwarteng, "Extracting spectral contrast in Landsat Thematic Mapper image data using selective principal component analysis," Photogrammetric Engineering and Remote Sensing, 55(3), 339-348 (1989); http://pubs.er.usgs.gov/publication/70015931.
[29] W. P. Loughlin, "Component Analysis for Alteration Mapping," Photogram. Eng. Rem. Sens., 57, 1163-1169 (1991).
[30] M. Julivert, "Decollement tectonics in the Hercynian Cordillera of Northwest Spain," American Journal of Science, 270(1), 1-29 (1971); doi: 10.2475/ajs.270.1.1.
[31] M. Z. Khedr, S. Kamh, A. A. Al Desouky, E. Takazawa, C. Hauzenberger, S. A. Whattam, and A. El-Awady, "Remote sensing and geochemical investigations of sulfide-bearing metavolcanic and gabbroic rocks (Egypt): Constraints on host-rock petrogenesis and sulfide genesis," Gondwana Research, 119, 282-312 (2023); doi: https://doi.org/10.1016/j.gr.2023.03.021.

[32] S. Zamzam, “Geological Controls and Prospectivity Mapping for Manganese Ore Deposits Using Predictive Modeling Comparison: An Integration of Outcrop and Remote Sensing Data, Sinai Microplate, Egypt,” Journal of Earth Science, 34(2), 588-608 (2023); doi: 10.1007/s12583-021-1583-z.